Available online at www.sciencedirect.com
ScienceDirect
Acta Materialia 59 (2011) 1068–1076
Acta MATERIALIA
www.elsevier.com/locate/actamat

Thermodynamic modeling of the stacking fault energy of austenitic steels

S. Curtze [a,*], V.-T. Kuokkala [a], A. Oikari [b], J. Talonen [c], H. Hänninen [b]

[a] Tampere University of Technology, Department of Materials Science, P.O. Box 589, FI-33101 Tampere, Finland
[b] Aalto University School of Science and Technology, Department of Engineering Design and Production, P.O. Box 14200, FI-00076 Aalto, Finland
[c] Outokumpu Oyj, P.O. Box 140, FI-02201 Espoo, Finland

Received 14 September 2010; received in revised form 15 October 2010; accepted 17 October 2010
Available online 8 November 2010

Abstract

The stacking fault energies (SFE) of 10 austenitic steels were determined in the temperature range $50 \leqslant T \leqslant 600$ K by thermodynamic modeling of the Fe–Cr–Ni–Mn–Al–Si–Cu–C–N system using a modified Olson and Cohen modeling approach (Olson GB, Cohen M. Metall Trans 1976;7A:1897 [1]). The applied model accounts for each element's contribution to the Gibbs energy, the first-order excess free energies, magnetic contributions and the effect of interstitial nitrogen. Experimental SFE values from X-ray diffraction measurements were used for comparison. The effect of SFE on deformation mechanisms was also studied by electron backscatter diffraction.

Keywords: Austenitic steel; Stacking fault energy; Thermodynamic modeling; Electron backscatter diffraction (EBSD)

1. Introduction

In face-centered cubic (fcc) metals, the stacking fault energy γ_{SFE} is one of the most important parameters determining which deformation and/or transformation mechanism(s) will occur during plastic straining of the material. Consequently, the stacking fault energy can affect quite strongly the mechanical behavior of these materials. At low γ_{SFE}, wide dissociation of dislocations into Shockley partials can hinder dislocation glide and thus favor mechanical twinning ($\gamma \rightarrow \gamma'_T$) or martensitic phase transformations ($\gamma_{fcc} \rightarrow \varepsilon^{Ms}_{hcp}$ or $\gamma_{fcc} \rightarrow (\varepsilon^{Ms}_{hcp}) \rightarrow \alpha'^{Ms}_{bcc}$). In general, the relative values of stacking fault energy, where α' or ε-martensite formation, twinning or slip govern the plastic deformation process, are $\gamma^{\varepsilon,\alpha'}_{SFE} < \gamma^{T}_{SFE} < \gamma^{slip}_{SFE}$ [1–3]. According to numerous investigations, α'-martensite nucleates at the intersection of shear bands [1–5]. Therefore, as shear bands in austenitic steels with low SFE consist of more or less perfect ε-martensite [6], the presence of ε-martensite is often considered a prerequisite for the formation of α'-martensite. At lower SFE, the probability for the presence of appropriate arrays of partial dislocations is increased, and hence more α'-martensite nucleation sites are available [1,3]. According to Lecroisey and Pineau [5], α'-martensite nucleation can also occur at the intersection of a Shockley partial dislocation and a deformation twin. However, since the self-energy of the dislocation is increased in that case, the reaction requires additional energy. This energy can be provided, for example, by the energy released upon the $\gamma \rightarrow \alpha'$ phase transformation due to the difference in the Gibbs energies of the two phases, or by the assistance of local stress concentrations.

In the present study, the thermodynamic modeling approach originally proposed by Olson and Cohen [1] was adopted to calculate the ideal stacking fault energy γ_{SFE} for the Fe–Cr–Ni–Mn–Al–Si–Cu–C–N system over a wide range of temperatures. The thermodynamic datasets needed for the calculations were acquired from the literature and implemented into a Matlab code, which was programmed for this purpose. The applicability of the model was verified in two ways: by direct comparison of the

* Corresponding author. Tel.: +358 44 3131 595.
E-mail address: sven.curtze@oxinst.com (S. Curtze).

1359-6454/$36.00
doi:10.1016/j.actamat.2010.10.037

calculated SFE values with those obtained from X-ray diffraction (XRD) measurements, and by studying the materials' propensities to stress or strain induced phase transformations and/or twinning by analyzing pre-strained specimens with the electron backscatter diffraction (EBSD) technique.

1.1. Thermodynamic modeling of the SFE

The flowchart in Fig. 1 shows a summary of the equations forming the basis of the present model. A detailed description of the model can be found, for example, in Ref. [7]. In the present paper, only the modifications and extensions made to the basic model are described more thoroughly, such as the implementation of the effect of nitrogen and the changes in the model due to the additional substitutional alloying elements Cr, Ni and Cu. The chemical compositions of the materials for which SFE calculations were performed are presented in Table 1. The materials include two chromium–nickel alloyed stainless steels, seven chromium–manganese–nickel–nitrogen alloyed stainless steels and one high manganese TWIP steel.

The main assumption of the model originally proposed by Olson and Cohen [1] is that a stacking fault in an fcc crystal structure is basically a thin layer of hexagonal close-packed (hcp) phase, separated from the matrix by a phase boundary on each side. The ideal stacking fault energy γ_{SFE} is then expressed by

$$\gamma_{SFE} = 2\rho\Delta G^{\gamma\to\varepsilon} + 2\sigma \quad (1)$$

where ρ is the molar surface density along {1 1 1} planes, $\Delta G^{\gamma\to\varepsilon}$ is the molar Gibbs energy of the austenite to ε-martensite phase transformation $\gamma_{fcc} \to \varepsilon^{Ms}_{hcp}$ and σ is the interfacial energy per unit area of the phase boundary. It is

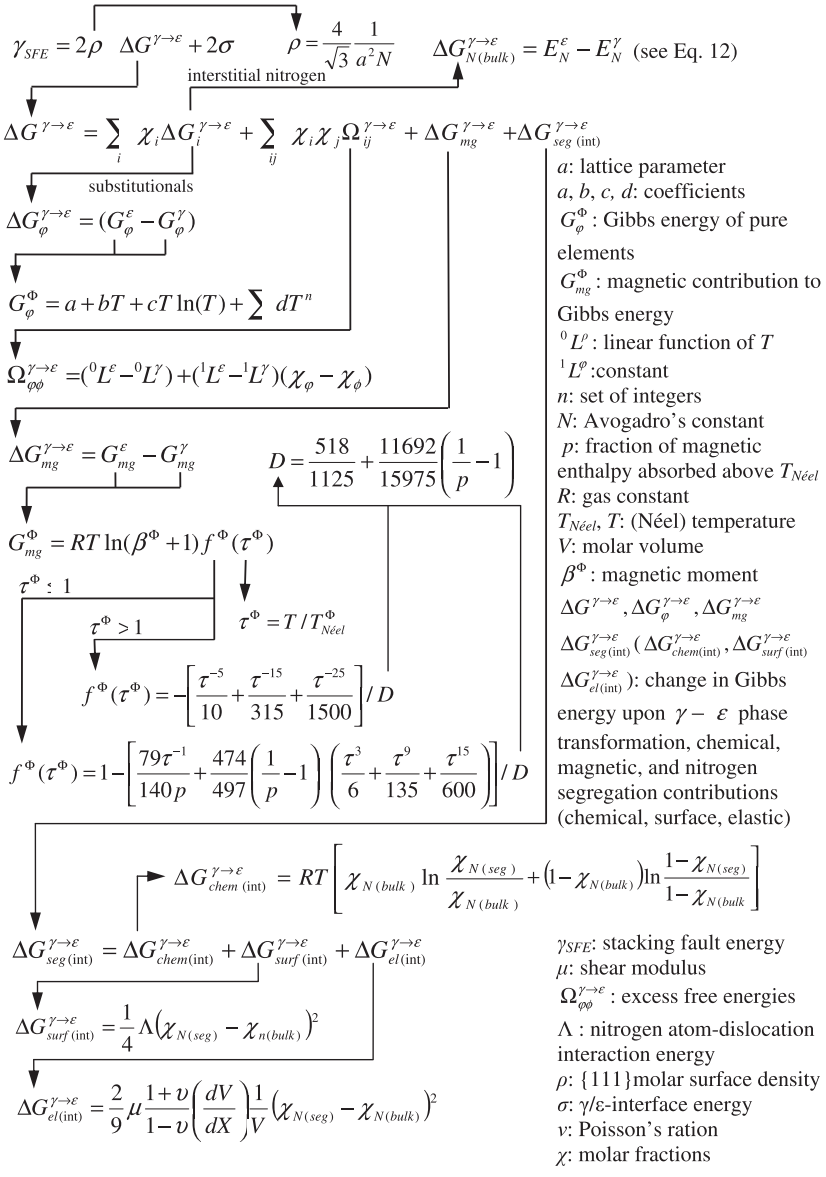

Fig. 1. Flow chart of the thermodynamic SFE calculations.

Table 1
Chemical compositions of the materials for which the SFE calculations were performed (in wt.%).

Grade	C	Si	Mn	Cr	Ni	Al	Cu	N	Fe	Calculated γ_{SFE}^{RT}	Measured γ_{SFE}^{RT}
1.4301	0.049	0.43	1.49	18.2	8.2	0.003	0.43	0.047	Bal.	30.0	
1.4301-1	0.041	0.33	1.71	18.2	8.1		0.37	0.054	Bal.	29.2	17.8 ± 1.2
1.4310	0.093	1.12	1.22	16.7	6.4	0.002	0.25	0.074	Bal.	26.6	
1.4372	0.045	0.35	6.97	17.6	4.5	0.005	0.25	0.198	Bal.	24.6	
1.4318	0.030	0.50	1.23	17.4	6.6		0.168	0.168	Bal.	23.7	
1.4318-1	0.019	0.48	1.61	17.6	6.6		0.22	0.094	Bal.	23.2	12.8 ± 1.5
1.4318-2	0.017	0.51	1.34	17.4	6.6		0.14	0.145	Bal.	22.6	14.7 ± 0.8
TWIP-1	0.08	0.28	28.0	<0.01		1.6			Bal.	27.0	
201Cu	0.047	0.29	5.70	17.3	4.7	0.001	2.39	0.107	Bal.	24.9	
204Cu	0.079	0.40	9.00	15.2	1.1	0.002	1.68	0.115	Bal.	16.8	

Test heats are designated with an additional number after the EN standard code, e.g. 1.4301-1.

assumed that the system is a regular solid solution of atoms in substitutional lattice sites and interstitial atoms in the octahedral sites of the fcc and hcp crystal structures.

In the present study, the lattice parameter a required to calculate the molar surface density ρ was determined from XRD measurements on the studied steel grades using Ge-filtered Co Kα radiation. An average value $a = 3.60 \pm 0.01$ Å was obtained for all grades. The lattice parameter a was assumed to be independent of temperature, which is a reasonable approximation since the variation in a for comparable materials is typically of the order ± 0.01 Å in the temperature range in question [8], and therefore its effect on γ_{SFE} is negligible. The energy per surface unit of the {1 1 1} interface between ε and γ phases was assumed to be $\sigma = 8$ mJ m^{-2}, which is a typical value reported for comparable chemical compositions [1,9,10].

In the present model, the term $\Delta G^{\gamma\to\varepsilon}$ in Eq. (1) accounts for the change in the Gibbs energy $\Delta G_{\rho}^{\gamma\to\varepsilon}$ of each element φ upon the $\gamma_{fcc} \to \varepsilon_{hcp}^{Ms}$ phase transformation, the excess free energies $\Omega_{\varphi\phi}^{\gamma\to\varepsilon}$, i.e. the first-order interactions between elements φ and ϕ, magnetic contributions to the Gibbs energy $\Delta G_{mg}^{\gamma\to\varepsilon}$, and the effect of interstitial nitrogen. Hence, the change in the molar Gibbs energy $\Delta G^{\gamma\to\varepsilon}$ can be written as

$$\Delta G^{\gamma\to\varepsilon} = \sum_i \chi_i \Delta G_i^{\gamma\to\varepsilon} + \sum_{ij} \chi_i \chi_j \Omega_{ij}^{\gamma\to\varepsilon} + \Delta G_{mg}^{\gamma\to\varepsilon} + \Delta G_{seg(\mathrm{int})}^{\gamma\to\varepsilon} \quad (2)$$

with χ the molar fractions of the pure alloying elements.

The first three terms of Eq. (2) have been described thoroughly in Ref. [7]. The thermodynamic datasets needed for the calculations were acquired from the literature, mostly from publications of CALPHAD studies. Table 2 summarizes the datasets used in the present study.

The magnetic contribution $\Delta G_{mg}^{\gamma\to\varepsilon}$ to the change in the Gibbs energy $\Delta G^{\gamma\to\varepsilon}$ due to the Néel transition of each phase Φ, i.e. the paramagnetic-to-antiferromagnetic transition, was calculated by

$$\Delta G_{mg}^{\gamma\to\varepsilon} = G_{mg}^{\varepsilon} - G_{mg}^{\gamma} \quad (3)$$

The magnetic contribution to the Gibbs energy G of each phase Φ, G_{mg}^{Φ}, was calculated following Hillert and Jarl's [11] modification of the model proposed by Inden [12] as

Table 2
Functions describing the change in the Gibbs energy $\Delta G_{\varphi}^{\gamma\to\varepsilon}$ upon the $\gamma_{fcc} \to \varepsilon_{hcp}^{Ms}$ phase transformation for the pure elements Fe, Mn, Cr, Ni, Cu, Al and Si, the excess energy coefficients $\Omega_{\varphi\phi}^{\gamma\to\varepsilon}$ used in the study, the empirical formula describing the effect of carbon on $\Delta G^{\gamma\to\varepsilon}$, and both the bulk and segregation contributions by N.

Parameter	Function (J mol^{-1})	Reference
$\Delta G_{Fe}^{\gamma\to\varepsilon}$	$-2243.38 + 4.309\ T$	[17]
$\Delta G_{Mn}^{\gamma\to\varepsilon}$	$-1000.00 + 1.123\ T$	[17]
$\Delta G_{Cr}^{\gamma\to\varepsilon}$	$1370–0.163\ T$	[12,17]
$\Delta G_{Ni}^{\gamma\to\varepsilon}$	$1046 + 1.255\ T$	[17]
$\Delta G_{Cu}^{\gamma\to\varepsilon}$	$600 + 0.2\ T$	[17]
$\Delta G_{Al}^{\gamma\to\varepsilon}$	$2800 + 5\ T$	[12]
$\Delta G_{Si}^{\gamma\to\varepsilon}$	$-560–8\ T$	[12]
$\Delta G_{N(bulk)}^{\gamma\to\varepsilon}$	See Eq. (18)	[2]
$\Delta G_{seg(\mathrm{int})}^{\gamma\to\varepsilon}$	See Eq. (19)–(25)	[2,4,5,7]
$\Delta G_{FeMnX/C}^{\gamma\to\varepsilon}$	$\frac{1246}{\chi_C}(1 - \exp(-24.29\chi_C)) - 17.175\chi_{Mn}$	[12]
$\Omega_{FeMn}^{\gamma\to\varepsilon}$	$2873–717\ (\chi_{Fe} - \chi_{Mn})$	[19]
$\Omega_{FeCr}^{\gamma\to\varepsilon}$	2095	[15]
$\Omega_{FeNi}^{\gamma\to\varepsilon}$	2095	[15]
$\Omega_{FeAl}^{\gamma\to\varepsilon}$	3328	[19]
$\Omega_{FeSi}^{\gamma\to\varepsilon}$	$2850 + 3520\ (\chi_{Fe} - \chi_{Si})$	[12]
$\Omega_{CrNi}^{\gamma\to\varepsilon}$	4190	[15]

$$G_{mg}^{\Phi} = RT\ln(\beta^{\Phi} + 1) f^{\Phi}(\tau^{\Phi}) \quad (4)$$

with R the gas constant, T the temperature, β^{Φ} the magnetic moment of phase Φ divided by the Bohr magneton μ_B, and $f^{\Phi}(\tau^{\Phi})$ a polynomial function of the scaled Néel temperature $\tau^{\Phi} = T/T_{Néel}^{\Phi}$ [11]. The magnetic moment of the austenite phase was calculated using the weighted sums of the pure elements' magnetic moments

$$\beta^{\gamma} = \chi_{Fe}\beta_{Fe} + \chi_{Mn}\beta_{Mn} + \chi_{Ni}\beta_{Ni} - \chi_{Cr}\beta_{Cr} - \chi_{Fe}\chi_{Mn+Ni}\beta_{FeMn/Ni} - \chi_C\beta_C \quad (5)$$

where β_{Fe}, β_{Mn}, β_{Ni} and β_{Cr} are empirical values for the magnetic moments of the pure elements and $\beta_{FeMn/Ni}$ is a second order term originally proposed by Cotes et al. [13] for the binary Fe–Mn system, which takes account for the deviation from generic mixture behavior. In Eq. (5), the influence of carbon was introduced by the additional term $(-\chi_C\beta_C)$, as proposed by Dumay et al. [14]. The influence of Al, Si and Cu on the magnetic moment was not taken into consideration, neither that of N, which has only a

minor effect on $\Delta G_{mg}^{\gamma\to\varepsilon}$ [15]. According to Huang [16], the values for β_{Fe} and β_{Mn} are 0.7 and 0.62, respectively, and the values for β_{Ni} and β_{Cr} are 0.62 [17] and 0.8 [11], respectively. The values $\beta_{FeMn} = 0.64$ and $\beta_C = 4$ were taken from Dumay et al. [14]. The magnetic moment of the ε phase was calculated according to Huang [16] with the additional term proposed by Dumay et al. [14] as

$$\beta^{\varepsilon} = \chi_{Mn}\beta_{Mn} - \chi_C\beta_C \tag{6}$$

The magnetic transition temperature $T_{Néel}^{\Phi}$ was calculated according to the empirical expressions presented in Ref. [18]. For $T_{Néel}^{\gamma}$, an additional term was needed to take into account the effect of Ni on the Néel temperature. This term was obtained by a linear fit of empirical $T_{Néel}^{\gamma}$ data at varying Ni concentrations taken from the literature [18,19], so that

$$T_{Néel}^{\gamma} = 251.71 + 681\chi_{Mn} - 272\chi_{Cr} - 1800\chi_{Ni} - 1151\chi_{Al} - 1575\chi_{Si} - 1740\chi_C \tag{7}$$

and

$$T_{Néel}^{\varepsilon} = 580\chi_{Mn} \tag{8}$$

The formulas for β^{Φ}/μ_B and the Néel temperature $T_{Néel}^{\Phi}$ are summarized in Table 3.

In order to include also the contribution of nitrogen in the stacking fault energy calculations, the approach presented by Yakubtsov et al. [15] was adopted. Nitrogen contributes to the Gibbs energy change in two ways: by a bulk effect and by a segregation effect due to the segregation of nitrogen to stacking faults. The bulk effect arises from the interaction of nitrogen with alloying elements in the substitutional lattice sites. Its contribution to the change in Gibbs energy can be included in the first summation term of Eq. (2) by adding $\Delta G_{N(bulk)}^{\gamma\to\varepsilon}$. The contribution arising from nitrogen segregation to stacking faults is taken into account by the last term in Eq. (2).

1.2. Calculation of nitrogen contribution to the change in Gibbs energy

The bulk contribution to the change in Gibbs energy arising from interstitial nitrogen atoms is taken into account by calculating the change in the configurational energies of interstitial nitrogen atoms surrounded by atoms in substitutional lattice sites upon the $\gamma_{fcc} \to \varepsilon_{hcp}^{Ms}$ phase transformation, i.e.

$$\Delta G_{N(bulk)}^{\gamma\to\varepsilon} = E_N^{\varepsilon} - E_N^{\gamma} \tag{9}$$

where E_N^{ε} and E_N^{γ} are the configurational energies of interstitial nitrogen in the ε and γ phases, respectively. In the present study, only the first nearest neighbor interaction energies between interstitial and substitutional atoms were considered in the calculations of E_N^{Φ}, and substitutional sites were only occupied by the four major elemental components, i.e. Fe, Mn, Cr and Ni, hence

$$E_N^{\Phi} = \sum_{m=0}^{6}\sum_{i=0}^{6-j-k-l}\sum_{j=0}^{6-k-l}\sum_{k=0}^{6-l}\sum_{l}^{6}\Big[(n_1)_i U_{1N}^{\Phi} + (n_2)_j U_{2N}^{\Phi} + (n_3)_k U_{3N}^{\Phi} + (n_4)_l U_{4N}^{\Phi}\Big](n_N)_m \tag{10}$$

where $(n_{1\ldots4})_{i\ldots l}$ is the number of atoms of each type of substitutional element $1\ldots4$ occupying the substitutional lattice sites in the alloy, $U_{1\ldots4N}^{\Phi}$ is the interaction energy between each type of substitutional element and interstitial nitrogen, n_N is the number of nitrogen atoms in interstitial sites per unit cell and m is the number of interstitial (octahedral) sites in each unit cell of phase Φ. Since

$$(n_1)_i + (n_2)_j + (n_3)_k + (n_4)_l = 6 \tag{11}$$

and hence

$$(n_2)_j = 6 - (n_1)_i - (n_3)_k - (n_4)_l \tag{12}$$

one can substitute $(n_2)_j$ in Eq. (10) by Eq. (12), which leads to

$$E_N^{\Phi} = \sum_{m=0}^{6}\sum_{i=0}^{6-j-k-l}\sum_{j=0}^{6-k-l}\sum_{k=0}^{6-l}\sum_{l}^{6}\Big[(n_1)_i U_{1N}^{\Phi} + (6-(n_1)_i - \big((n_3)_k - (n_4)_l\big)_j U_{2N}^{\Phi} + (n_3)_k U_{3N}^{\Phi} + (n_4)_l U_{4N}^{\Phi}\Big](n_N)_m \tag{13}$$

By rearranging the terms one obtains

$$E_N^{\Phi} = (U_{1N}^{\Phi} - U_{2N}^{\Phi})\sum_{m=0}^{6}\sum_{i=0}^{6-j-k-l}(n_1)_i(n_N)_m + (U_{3N}^{\Phi} - U_{2N}^{\Phi})\sum_{m=0}^{6}\sum_{l=0}^{6}(n_3)_l(n_N)_m + (U_{4N}^{\Phi} - U_{2N}^{\Phi})\sum_{m=0}^{6}\sum_{k=0}^{6-l}(n_4)_k(n_N)_m + 6U_{2N}^{\Phi}\sum_{m=6}^{6}(n_N)_m \tag{14}$$

As shown by Smirnov [20], the following equation is valid for close packed crystal structure alloy systems with nitrogen as interstitial alloying element and $1\ldots Z$ elements occupying the substitutional lattice sites [15]:

Table 3
The formulas for β^{Φ}/μ_B and the Néel temperature $T_{Néel}^{\Phi}$ (in K).

Parameter	Function	Reference
$T_{Néel}^{\gamma}$	$T_{Néel}^{\gamma} = 251.71 + 681\chi_{Mn} - 272\chi_{Cr} - 1800\chi_{Ni} - 1151\chi_{Al} - 1575\chi_{Si} - 1740\chi_C$	[11] modified
$T_{Néel}^{\varepsilon}$	$580\chi_{Mn}$	[16]
β^{γ}	$\chi_{Fe}0.7 + \chi_{Mn}0.62 + \chi_{Ni}0.62 - \chi_{Cr}0.8 - \chi_{Fe}\chi_{Mn}0.64 - \chi_C 4$	[7,12,16,21] modified
β^{ε}	$\chi_{Mn}0.62 - \chi_C 4$	[12,16]

$$\sum_{m=0}^{6}\sum_{i=0}(n_1)_i(n_N)_m = \frac{6\chi_N\chi_1\exp\frac{U^{\Phi}_{1N}}{RT}}{\sum_Z \chi_Z \exp\frac{U^{\Phi}_{ZN}}{RT}} \tag{15}$$

while

$$\sum_Z \chi_Z = 1 \tag{16}$$

where χ_1 and χ_Z are the molar fractions of atoms $1 \ldots Z$ occupying the substitutional lattice sites, and χ_N the molar fraction of nitrogen. For the present case of an alloy system with four types of atoms occupying the substitutional lattice sites and nitrogen in the interstitial sites, Eq. (14) can be rewritten as

$$\begin{aligned} E^{\Phi}_N = {} & 6\chi_N U^{\Phi}_{2N} + \left(U^{\Phi}_{1N} - U^{\Phi}_{2N}\right)\frac{6\chi_N\chi_1\exp\frac{U^{\Phi}_{1N}}{RT}}{\sum_{Z=1}^{4}\chi_Z\exp\frac{U^{\Phi}_{ZN}}{RT}} \\ & + \left(U^{\Phi}_{3N} - U^{\Phi}_{2N}\right)\frac{6\chi_N\chi_3\exp\frac{U^{\Phi}_{3N}}{RT}}{\sum_{Z=1}^{4}\chi_Z\exp\frac{U^{\Phi}_{ZN}}{RT}} \\ & + \left(U^{\Phi}_{4N} - U^{\Phi}_{2N}\right)\frac{6\chi_N\chi_4\exp\frac{U^{\Phi}_{4N}}{RT}}{\sum_{Z=1}^{4}\chi_Z\exp\frac{U^{\Phi}_{ZN}}{RT}} \end{aligned} \tag{17}$$

Recalling Eq. (9) and replacing the configurational energies E^{ε}_N and E^{γ}_N of interstitial nitrogen in the ε and γ phase, respectively, by the expression in Eq. (17), one obtains the expression for the change in Gibbs energy arising from interstitial nitrogen upon the $\gamma_{fcc} \rightarrow \varepsilon^{Ms}_{hcp}$ phase transformation:

$$\begin{aligned} \Delta G^{\gamma\to\varepsilon}_{N(bulk)} = {} & E^{\varepsilon}_N - E^{\gamma}_N \\ = {} & 6\left[\left(U^{\varepsilon}_{2N} - U^{\gamma}_{2N}\right) + \frac{\left(U^{\varepsilon}_{1N} - U^{\varepsilon}_{2N}\right)\chi_1}{\chi_1 + \chi_2\exp\left[-\frac{\left(U^{\varepsilon}_{1N}-U^{\varepsilon}_{2N}\right)}{RT}\right] + \chi_3\exp\left[-\frac{\left(U^{\varepsilon}_{1N}-U^{\varepsilon}_{3N}\right)}{RT}\right] + \chi_4\exp\left[-\frac{\left(U^{\varepsilon}_{1N}-U^{\varepsilon}_{4N}\right)}{RT}\right]}\right. \\ & + \frac{\left(U^{\varepsilon}_{3N} - U^{\varepsilon}_{2N}\right)\chi_3}{\chi_1\exp\left[-\frac{\left(U^{\varepsilon}_{3N}-U^{\varepsilon}_{1N}\right)}{RT}\right] + \chi_2\exp\left[-\frac{\left(U^{\varepsilon}_{3N}-U^{\varepsilon}_{2N}\right)}{RT}\right] + \chi_3 + \chi_4\exp\left[-\frac{\left(U^{\varepsilon}_{3N}-U^{\varepsilon}_{4N}\right)}{RT}\right]} \\ & + \frac{\left(U^{\varepsilon}_{4N} - U^{\varepsilon}_{2N}\right)\chi_4}{\chi_1\exp\left[-\frac{\left(U^{\varepsilon}_{4N}-U^{\varepsilon}_{1N}\right)}{RT}\right] + \chi_2\exp\left[-\frac{\left(U^{\varepsilon}_{4N}-U^{\varepsilon}_{2N}\right)}{RT}\right] + \chi_3\exp\left[-\frac{\left(U^{\varepsilon}_{4N}-U^{\varepsilon}_{3N}\right)}{RT}\right] + \chi_4} \\ & - \frac{\left(U^{\gamma}_{1N} - U^{\gamma}_{2N}\right)\chi_1}{\chi_1 + \chi_2\exp\left[-\frac{\left(U^{\gamma}_{1N}-U^{\gamma}_{2N}\right)}{RT}\right] + \chi_3\exp\left[-\frac{\left(U^{\gamma}_{1N}-U^{\gamma}_{3N}\right)}{RT}\right] + \chi_4\exp\left[-\frac{\left(U^{\gamma}_{1N}-U^{\gamma}_{4N}\right)}{RT}\right]} \\ & - \frac{\left(U^{\gamma}_{3N} - U^{\gamma}_{2N}\right)\chi_3}{\chi_1\exp\left[-\frac{\left(U^{\gamma}_{3N}-U^{\gamma}_{1N}\right)}{RT}\right] + \chi_2\exp\left[-\frac{\left(U^{\gamma}_{3N}-U^{\gamma}_{2N}\right)}{RT}\right] + \chi_3 + \chi_4\exp\left[-\frac{\left(U^{\gamma}_{3N}-U^{\gamma}_{4N}\right)}{RT}\right]} \\ & \left. - \frac{\left(U^{\gamma}_{4N} - U^{\gamma}_{2N}\right)\chi_4}{\chi_1\exp\left[-\frac{\left(U^{\gamma}_{4N}-U^{\gamma}_{1N}\right)}{RT}\right] + \chi_2\exp\left[-\frac{\left(U^{\gamma}_{4N}-U^{\gamma}_{2N}\right)}{RT}\right] + \chi_3\exp\left[-\frac{\left(U^{\gamma}_{4N}-U^{\gamma}_{3N}\right)}{RT}\right] + \chi_4}\right] \end{aligned} \tag{18}$$

Eq. (18) requires empirical values for the difference in the interaction energies between each nitrogen-substitutional alloying element pair in both fcc and hcp structures. The values for the γ phase are summarized in Table 4. For the calculation of the corresponding ε phase values, one can make use of the expression proposed by Kaufman and Bernstein [21] and Ishikawa and Endoh [22]:

$$U^{\varepsilon}_{ij} = \Delta G^{\gamma\to\varepsilon}_i + U^{\gamma}_{ij} \tag{19}$$

where the subscript i stands for the major alloying element, such that, for example

Table 4
The numerical values for the difference in interaction energies between each nitrogen-substitutional alloying element pair in the fcc structure.

Thermodynamic term	Numerical value (J mol^{-1})	Reference
$U^{\gamma}_{FeN} - U^{\gamma}_{CrN}$	18.800	[13]
$U^{\gamma}_{FeN} - U^{\gamma}_{NiN}$	−17.000	[13]
$U^{\gamma}_{CrN} - U^{\gamma}_{NiN}$	35.800	[13]
$U^{\gamma}_{FeN} - U^{\gamma}_{MnN}$	8.800	[13]
$U^{\gamma}_{CrN} - U^{\gamma}_{MnN}$	−10.000	[13]
$U^{\gamma}_{NiN} - U^{\gamma}_{MnN}$	25.800	[13]

$$U^{\gamma}_{FeN} - U^{\gamma}_{NiN} = \left(U^{\varepsilon}_{FeN} - U^{\varepsilon}_{NiN}\right) + \left(\Delta G^{\gamma\to\varepsilon}_{Fe} - \Delta G^{\gamma\to\varepsilon}_{Ni}\right) \tag{20}$$

Expressions for the other pairs of interacting elements can be obtained correspondingly. The first term in Eq. (18), i.e. $(U^{\varepsilon}_{2N} - U^{\gamma}_{2N})$, can also be derived from Eq. (19), which then becomes $\Delta G^{\gamma\to\varepsilon}_i$.

The change in Gibbs energy due to the segregation of nitrogen to stacking faults $\Delta G^{\gamma\to\varepsilon}_{seg(int)}$ can be divided into three parts [15,7]: the chemical Gibbs energy due to Suzuki segregation $\Delta G^{\gamma\to\varepsilon}_{chem(int)}$, the surface Gibbs energy $\Delta G^{\gamma\to\varepsilon}_{surf(int)}$ due to the concentration difference between the matrix and stacking faults, and the elastic Gibbs energy $\Delta G^{\gamma\to\varepsilon}_{el(int)}$, arising from the segregation of elements with different atomic sizes, such that

$$\Delta G^{\gamma\to\varepsilon}_{seg(int)} = \Delta G^{\gamma\to\varepsilon}_{chem(int)} + \Delta G^{\gamma\to\varepsilon}_{surf(int)} + \Delta G^{\gamma\to\varepsilon}_{el(int)} \tag{21}$$

According to Ishida [17], $\Delta G^{\gamma\to\varepsilon}_{chem(int)}$ can be calculated as

$$\Delta G^{\gamma\to\varepsilon}_{chem(int)} = RT\left[\chi_{N(bulk)}\ln\frac{\chi_{N(seg)}}{\chi_{N(bulk)}} + \left(1-\chi_{N(bulk)}\right)\ln\frac{1-\chi_{N(seg)}}{1-\chi_{N(bulk)}}\right] \tag{22}$$

The concentration of nitrogen on stacking faults $\chi_{N(seg)}$ can be calculated from the concentration of nitrogen in the bulk $\chi_{N(bulk)}$, assuming that the equilibrium condition is satisfied, i.e. the chemical potentials of the γ and ε phases are the same such that

$$\frac{dG^{\gamma}}{d\chi_{N(bulk)}} = \frac{dG^{\varepsilon}}{d\chi_{N(seg)}} \tag{23}$$

where G^{γ} and G^{ε} are the free energies of the γ and ε phases, respectively [17]. For a binary alloy, Eq. (23) becomes

$$\begin{aligned} & -\Delta G^{\gamma\to\varepsilon}_{1(sub)} + \Delta G^{\gamma\to\varepsilon}_{N(int)} + \Delta U^{\gamma\to\varepsilon}_{1N} \\ & + 2\left(U^{\varepsilon}_{1N}\chi_{N(seg)} - U^{\gamma}_{1N}\chi_{N(bulk)}\right) + RT\ln\frac{1-\chi_{N(seg)}}{1-\chi_{N(bulk)}} = 0 \end{aligned} \tag{24}$$

However, since the interaction energies U^{Φ}_{XN} for nitrogen with the substitutional elements (Fe, Mn, Cr, Ni) are not available in the literature, the γ and ε phases were assumed to be ideal solutions (i.e. $U^{\gamma}_{XN} = U^{\varepsilon}_{XN} = 0$), following Ishida's [17] approach. Due to the absence of further thermodynamic data needed for the calculation of the concentration of nitrogen on stacking faults $\chi_{N(seg)}$, more simplifications have to be made [15]. Therefore, the estimation proposed by Yakubtsov et al. [15] was adopted in the present study with

$$\chi_{N(seg)} = \left[1 + \frac{1-\chi_{N(bulk)}}{\chi_{N(bulk)}} \exp\left(\frac{-\Lambda}{RT}\right)\right]^{-1} \quad (25)$$

where Λ is the interaction energy of nitrogen with a dislocation in the fcc structure.

For the calculation of the change in surface Gibbs energy $\Delta G^{\gamma\to\varepsilon}_{surf(\mathrm{int})}$, the expression from the work of Ericsson [23] was adopted:

$$\Delta G^{\gamma\to\varepsilon}_{surf(\mathrm{int})} = \frac{1}{4}\Lambda\left(\chi_{N(seg)} - \chi_{n(bulk)}\right)^2 \quad (26)$$

The interaction energy Λ of nitrogen with a dislocation in the fcc structure was obtained by fitting a linear function to empirical Λ values at fixed nitrogen contents taken from the literature [15,24]. The following expression for Λ was obtained:

$$\Lambda = 11,848 + 824\chi_N \quad (27)$$

The change in elastic energy $\Delta G^{\gamma\to\varepsilon}_{el(\mathrm{int})}$ associated with the segregation of atoms of different size to stacking faults can be described by the term proposed by Suzuki [25] as

$$\Delta G^{\gamma\to\varepsilon}_{el(\mathrm{int})} = \frac{2}{9}\mu\frac{1+\upsilon}{1-\upsilon}\left(\frac{dV}{dX}\right)\frac{1}{V}\left(\chi_{N(seg)} - \chi_{N(bulk)}\right)^2 \quad (28)$$

with μ the shear modulus, υ Poisson's ratio and V the molar volume of the alloy. The elastic Gibbs energy contribution to the total change in Gibbs energy upon $\gamma_{fcc} \to \varepsilon^{Ms}_{hcp}$ phase transformation is, however, negligible and was therefore neglected in the present study.

2. Results and discussion

All the microstructural studies described in the following were performed on sheet steels originally delivered in the annealed condition. The materials were deformed in uniaxial tensile tests at low strain rates (average strain rates $3\times10^{-4} \leqslant \dot{\varepsilon} \leqslant 10^{-3}\ s^{-1}$).

The stacking fault energy values γ^{RT}_{SFE} calculated at room temperature for all studied materials are shown in Table 1. Fig. 2 shows these values together with experimentally measured γ^{RT}_{SFE} values for some of the materials, and Fig. 3 illustrates the modeled stacking fault energies as a function of temperature. The experimental γ^{RT}_{SFE} values were determined using the XRD line broadening and diffraction line displacement analysis. This technique is reviewed and described in detail, e.g. by Reed and Schramm [26,27] and Talonen [6].

Although the thermodynamically calculated and experimentally determined stacking fault energies differ in terms of absolute values, the relative correlation appears to be reasonably good. The deviation in the level of the SFE values obtained by the two different methods can be assigned to two main reasons. On the one hand, the thermodynamic stacking fault energy model presented in this paper does not describe an intrinsic material property but rather the idealized stacking fault energy for an infinite stacking fault with negligible lattice distortions within the stacking fault. Unlike

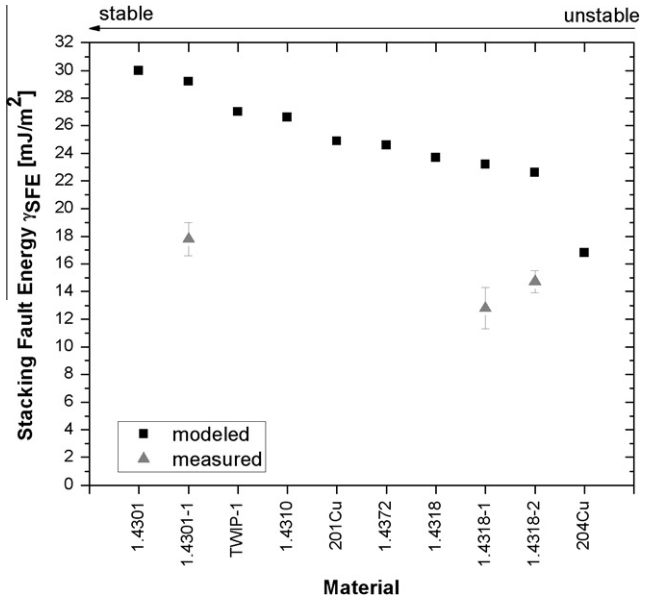

Fig. 2. Comparison of the modeled and measured room temperature SFEs γ^{RT}_{SFE} for selected materials. The error bars indicate the standard deviation of five XRD measurements and therefore represent the measurement reproducibility [32].

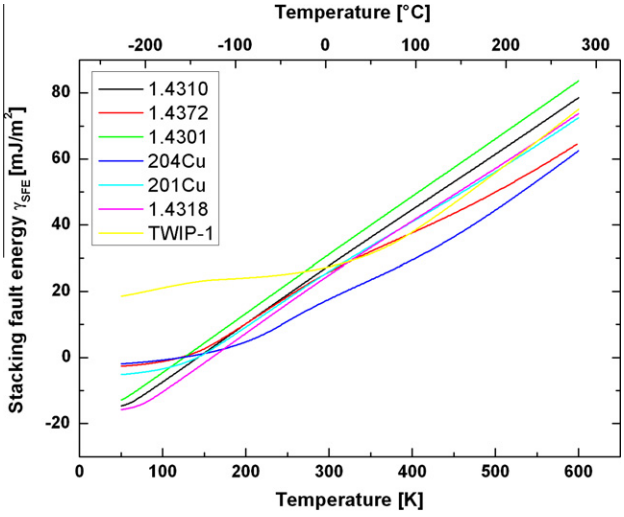

Fig. 3. The SFEs γ_{SFE} of the materials as a function of temperature. For better readability, the heats 1.4301-1, 1.4318-1 and 1.4318-2 were not included in the plot.

in real crystals, where dislocations and dislocation configurations, point defects, grain size and so forth can affect the stacking fault energy, these effects are not taken into account in the model. An attempt to take into consideration the effect of partial dislocations bounding the stacking fault was proposed by Müllner and Ferreira [28]. Studies by Jun and Choi [29] and Yang and Wan [30] investigated the correlation between the SFE and the austenite grain size, showing that the effect of the grain size becomes only of importance for small grain sizes. For larger grain sizes exceeding about 30 μm, the grain size effect reduces to less than 2 mJ m^{-2}

and saturates to zero for grain sizes around 150 μm [30]. Recent work by Saeed-Akbari et al. [31] confirmed these findings. On the other hand, both methods for determining the SFE are subject to quite considerable uncertainties due to measurement errors and lack of resolution in the XRD method, and assumptions and simplifications made in the calculations, which are discussed in more detail, for example, in Refs. [1,6,10,17,23,29,32–38].

At room temperature, the SFE of the 1.4301 stainless steel grade is highest of the studied materials, indicating rather high stability of the microstructure against martensite transformation, especially at low degrees of plastic deformation. EBSD scans on specimens deformed to 20% of engineering strain gave virtually no evidence of martensite transformation, with the exception of some small α'-martensite clusters present in shear bands and at twin boundaries.

Fig. 4a is an electron backscatter pattern (EBSP) quality map of the 1.4310 steel after 20% of engineering strain combined with phase identification maps for α'-martensite (colored in red) and ε-martensite (colored in yellow). Small ε-martensite phase fractions can be identified only in some shear bands, while smaller and larger arrays of α'-martensite are clearly present in quite many of the grains. The ε- and α'-martensite phase fractions were determined to be 0.14% and 6.15%, respectively.

In the high manganese TWIP steel, martensite formation was not observed at any stage of deformation. Initially, at low deformations, the thickness of deformation twins is also too low to be resolved by the EBSD technique. Only a few deformation twins were identified by the EBSD technique after 11% of tensile elongation, as can be seen in Fig. 5a, where twin boundaries are colored in yellow. However, at this stage of deformation the EBSP quality maps reveal shear bands in some of the grains, as can be seen in Fig. 5b. In the present case, the low band contrast signal obtained from the shear bands originates from the overlapping of the twin and matrix patterns, as Barbier et al. [38] have also shown in a study on high manganese TWIP steels. By deconvolution of the two patterns, the shear bands can be identified as twins. This procedure was adopted also in the present study and it confirmed the findings of Barbier et al. [38]. With increasing strain, the nanotwins stack up to bundles that can be resolved and indexed as twin domains by the EBSD technique. The actual thickness of the twins, however, is easily being overestimated due to the limitations in the spatial resolution of the EBSD technique. In fact, matrix laths remain between the stacked nanotwins, as transmission electron microscopy studies proved [39]. The twinning activity increases during further straining and secondary conjugate twin systems become active, as can be seen in Fig. 5c, where the EBSP quality map of TWIP 1 is shown after 30% of plastic deformation. Twins on conjugate slip planes form only after the tensile axis has rotated near to, or beyond, the $\langle 0\,0\,1\rangle - \langle \bar{1}\,1\,1\rangle$ symmetry line, where the primary and conjugate systems are equally stressed, as also predicted by theoretical considerations [33]. Fig. 5d shows the twinned

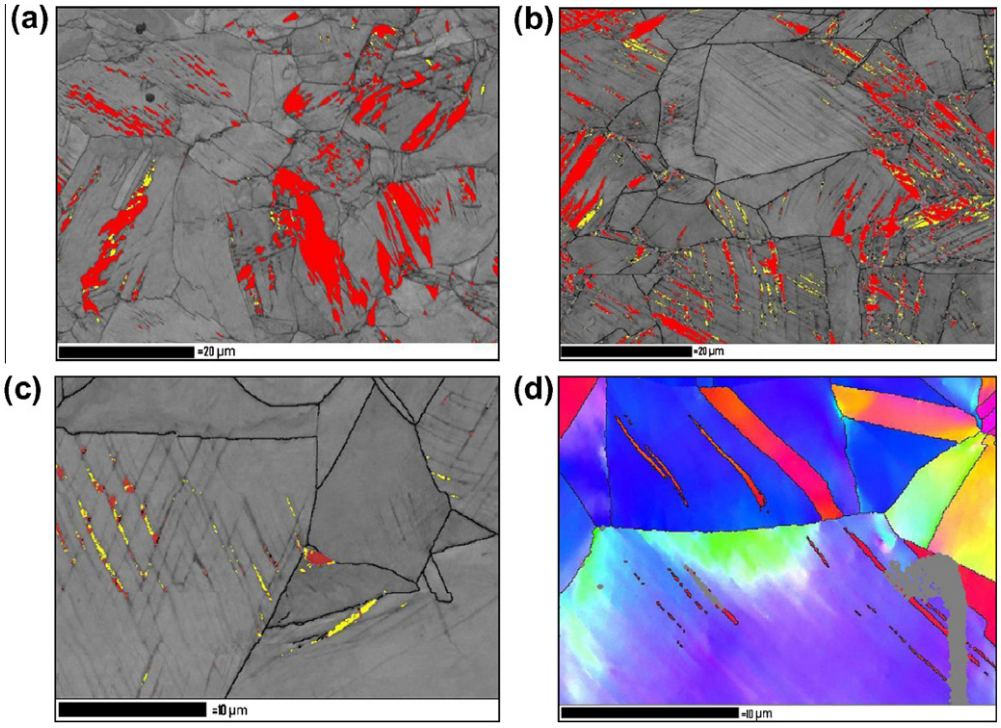

Fig. 4. EBSP quality map with ε- and α'-martensite phase identification maps of the 1.4310 steel after 20% plastic engineering strain (a), the 204Cu steel after 20% (b) and 10.5% (c) plastic engineering strain, and the orientation map of the 201Cu steel after 20% plastic engineering strain with twins colored in red (d). (For interpretation of the references to colour in this figure legend, the reader is referred to the web version of this article.)

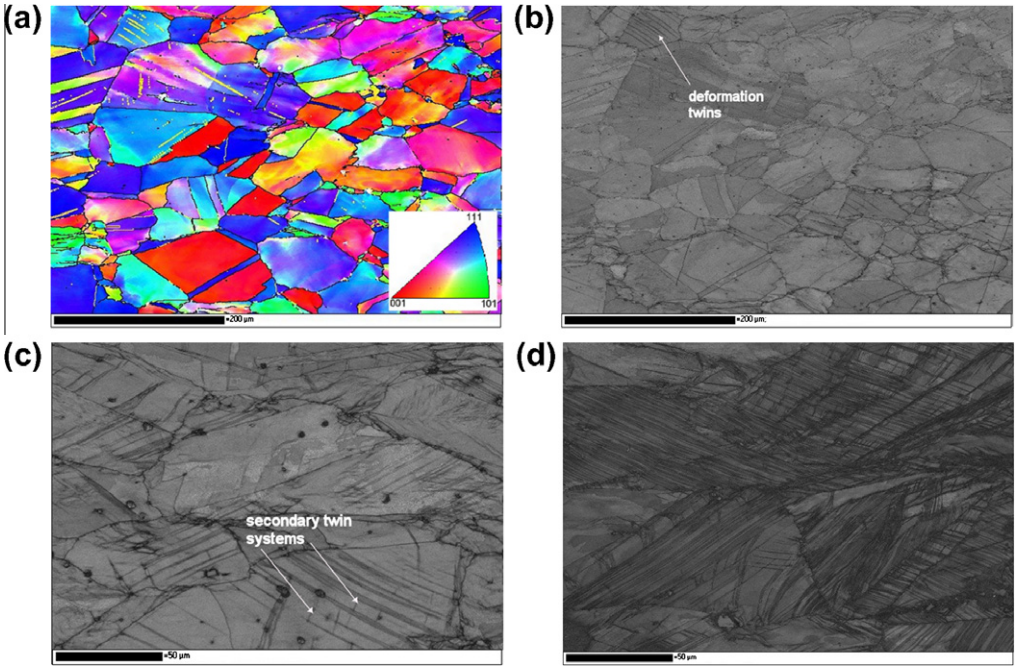

Fig. 5. Orientation map (IPF-x coloring scheme) (a) and EBSP quality map of the TWIP 1 steel after engineering strains of 11% (b), 35% (c) and 64% (d). (For interpretation of the references to colour in this figure legend, the reader is referred to the web version of this article.)

microstructure at fracture, where overlapping of twins with slip bands can be observed easily from the strong curvature of the twins, especially in heavily deformed sub-grain sections.

The 201Cu steel with a slightly lower SFE than the TWIP and the 1.4310 steel revealed only mechanical twinning after 20% engineering strain, and no martensite was detected, as can be seen from the EBSD orientation map in Fig. 4d. On the other hand, in the 204Cu steel, which had by far the lowest stacking fault energy of all studied materials, the ε- and α'-martensite phase fractions were higher than in any of the other materials at this stage of deformation. In particular, the tendency to form ε-martensite was highest in the 204Cu, indicating that the low SFE promotes formation of ε-martensite. Fig. 4b shows the EBSP quality map of the 204Cu steel together with the phase identification maps. The measured ε-martensite phase fraction was 1.5% and the α'-martensite phase fraction 9.6%. Compared to the 1.4310 grade, the phase fraction in ε-martensite is significantly higher in the 204Cu steel, whereas the α'-martensite phase fractions are of the same order of magnitude. Also the amount of shear bands in general appears to be larger in this steel compared with the other grades. It seems that ε-martensite is present in the shear bands while α'-martensite plates form at the shear band intersections. This observation is confirmed by Fig. 4c, which shows well the formation of ε-martensite in the shear bands and the formation of α'-martensite in the shear band intersections in the 204Cu steel after 10.5% engineering strain. Almost all sites revealing α'-martensite also reveal ε-martensite, strongly supporting the idea that α'-martensite nucleation preferentially takes place at the ε-martensite phase. Since the nucleation of α'-martensite requires an intersection of shear bands, α'-martensite will only form in grains where two conjugate slip band systems are activated. Therefore α'-martensite nucleation can be expected to also depend on the development of the deformation texture during plastic straining of the material.

3. Summary and Conclusions

A thermodynamic model for the calculation of the stacking fault energies of Fe–Cr–Ni–Mn–Al–Si–Cu–C–N austenitic steels was presented. The approach originally proposed by Olson and Cohen [1] was expanded with Yakubtsov et al.'s [15] proposal to account also for the effect of interstitial nitrogen. The SFE in the temperature range $50 \leqslant T \leqslant 600$ K was calculated for 10 austenitic steels and compared with XRD measurement results on some of these materials. The deformation mechanisms in selected grades were studied using EBSD.

- A good qualitative correlation between thermodynamically modeled and experimentally determined SFE values was obtained. Quantitatively, however, there was a systematic offset observed between the calculated and measured SFE values.
- The tendency for ε- and α'-martensite formation increased with decreasing SFE in good correlation with the modeled SFE values. In particular, the formation of ε-martensite was promoted by lower SFE. The twinning propensity was in general higher in steels with higher Mn contents, while in the Cr–Ni alloys martensite

transformations generally set in at higher SFE levels. A possible explanation for this is the higher driving energy towards α'-martensite formation due to a larger difference in the Gibbs energies of the γ and α' phases.

- ε-martensite was generally found in shear bands, while α'-martensite transformation occurred preferentially at shear band intersections.
- Twins on conjugate slip planes formed only after the tensile axis had rotated to or close to the $\langle 0\,0\,1\rangle$–$\langle \bar{1}\,1\,1\rangle$ symmetry line. This can also be expected for α'-martensite nucleation due to the requirement of intersecting slip bands for α'-martensite formation. The occurrence of twinning and of both ε- and α'-martensite transformation therefore seem to depend on the initial orientation of individual grains and on the development of the crystallographic texture during the deformation of fully austenitic steels.

Acknowledgements

This study was carried out as a part of the FIMECC (Finnish Metals and Engineering Competence Cluster) research program Light and Efficient Solutions supported by the Finnish Funding Agency for Technology and Innovation (Tekes). Tapio Saukkonen is gratefully acknowledged for conducting the EBSD scans on the stainless steel grades.

References

[1] Olson GB, Cohen M. Metall Trans 1976;7A:1897.
[2] Rémy L, Pineau A. Mater Sci Eng 1976;28(1):99–107.
[3] Olson GB, Cohen M. J Less Common Met 1972;28(1):107–18.
[4] Bogers AJ, Burgers WG. Acta Metall 1964;12(2):255–61.
[5] Lecroisey F, Pineau A. Metall Trans 1972;3(2):387–96.
[6] Talonen J. PhD thesis, Helsinki University of Technology; 2007. 125 p [TKK-DISS-2300].
[7] Curtze S, Kuokkala V-T. Acta Mater 2010;58(15):5129–41.
[8] Sumin VV, Simkin VG, Sheverev SG, Leont'eva-Smirnova MV, Chernov VM. Phys Met Metallogr 2009;108(6):600–5.
[9] Allain A, Chateau J-P, Bouaziz O, Migot S, Guelton N. Mater Sci Eng A 2004;387–389:158–62.
[10] Ferreira PJ, Müllner P. Acta Mater 1998;46(13):4479–84.
[11] Hillert M, Jarl M. CALPHAD 1978;2:227–38.
[12] Inden G. Phys B 1981;103:82–100.
[13] Cotes S, Sade M, Fernàndez Guillermet A. Metall Mater Trans A 1995;26A:1957–69.
[14] Dumay A, Chateau J-P, Allain S, Migot S, Bouaziz O. Mater Sci Eng A 2008;483–484:184–7.
[15] Yakubtsov IA, Ariapour A, Perovic DD. Acta Mater 1999;47(14):1271–9.
[16] Huang W. CALPHAD 1989;13:243–52.
[17] Ishida. Phys State Solid A 1976;36:717.
[18] Zhang YS, Lu X, Tian X, Qin Z. Mater Sci Eng A 2002;334:19–27.
[19] Chen S, Chung CY, Yan C, Hsu TY. Mater Sci Eng A 1999;264:262–8.
[20] Smirnov AA. Molekulyarno-kineticheskaya teoriya metallov [the molecular kinetic theory of metals]. Moskow: Nauka; 1966.
[21] Kaufman L, Bernstein H. Computer calculation of phase diagrams. New York: Academic Press; 1970.
[22] Ishikawa Y, Endoh Y. J Appl Phys 1968;39:1318–9.
[23] Ericsson T. Acta Metall 1966;14:1073.
[24] Hirth H, Cohen M. Metall Trans 1970:1.
[25] Suzuki H. Dislocation and mechanical properties of crystals. New York: Wiley; 1957.
[26] Reed RP, Schramm RE. J Appl Phys 1974;45(11):4705–11.
[27] Schramm RE, Reed RP. Metall Trans A 1975;6(7):1345–51.
[28] Müllner P, Ferreira PJ. Phil Mag Lett 1996;73(6):289–97.
[29] Jun J, Choi C. Mater Sci Eng A 1998;257:353–6.
[30] Yang WS, Wan CM. J Mater Sci 1990;25:1821–3.
[31] Saeed-Akbari A, Imlau J, Prahl U, Bleck W. Metall Mater Trans A 2009;40(13):3076–90.
[32] Petrov YN. Scripta Mater 2005;53:1201–6.
[33] Ko C, McLellan B. Acta Metall 1983;31(11):1821.
[34] Dinsdale AT. CALPHAD 1991;4(15):317–425.
[35] Dash J, Otte HM. Acta Metall 1963;11:1169.
[36] Dulieu D, Nutting J. ISI symposium SR86 1964;140.
[37] Miodownik AP. CALPHAD 1978;2(3):207–26.
[38] Barbier D, Gey N, Allain S, Bozzolo N, Humbert M. Mater Sci Eng A 2009;500:196–206.
[39] Curtze S, Kuokkala VT, Hokka M, Saarinen T. In: Conference proceedings the Dymat association, Brussels; 2009.